Structure-Determining Step in the Hierarchical Assembly of Peptoid Nanosheets

Babak Sanii,[†] Thomas K. Haxton, Gloria K. Olivier,[‡] Andrew Cho,[§] Bastian Barton,[⊥] Caroline Proulx, Stephen Whitelam, and Ronald N. Zuckermann*

The Molecular Foundry, Lawrence Berkeley National Laboratory, 1 Cyclotron Road, Berkeley, California 94720, United States. [†]Present address: Keck Science Department, Claremont McKenna, Scripps and Pitzer Colleges, Claremont, CA 91711. [‡]Present address: Agilent Technologies, Santa Clara, CA 95051. [§]Present address: Cornell Medical School, New York, NY 10065. [⊥]Present address: Gutenberg University Mainz, Welderweg 11, D-55099 Mainz, Germany.

ABSTRACT Organic two-dimensional nanomaterials are of growing importance, yet few general synthetic methods exist to produce them in high yields and to precisely functionalize them. We previously developed an efficient hierarchical supramolecular assembly route to peptoid bilayer nanosheets, where the organization of biomimetic polymer sequences is catalyzed by an air—water interface. Here we determine at which stages of assembly the nanoscale and atomic-scale order appear. We used X-ray scattering, grazing incidence X-ray scattering at the air—water interface, electron diffraction, and a recently developed computational coarse-grained peptoid model to probe the molecular ordering at various stages of assembly. We found that lateral packing and organization of the chains occurs during the formation of a peptoid monolayer, prior to its collapse into a bilayer. Identifying the structure-determining step enables strategies to influence nanosheet order, to predict and optimize production yields, and to further engineer this class of material. More generally, our results provide a guide for using fluid interfaces to catalytically assemble 2D nanomaterials.

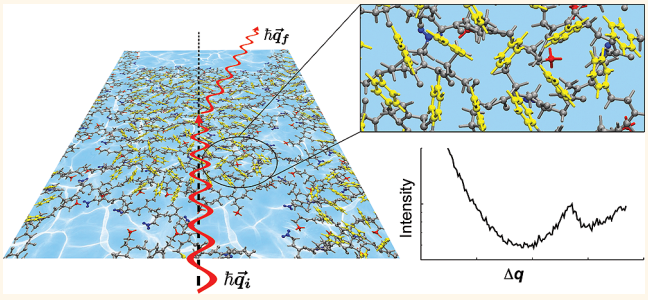

KEYWORDS: two-dimensional materials · supramolecular assembly · protein-mimetic materials · coarse-grained modeling · bioinspired polymers · interfacial assembly · monolayer compression

Two-dimensional (2D) nanomaterials are emerging as an important materials class with broad applications.[1] Their extreme aspect ratio gives rise to enormously high surface area to volume ratios, and to a variety of interesting biochemical, electrical, electrochemical, mechanical and photonic properties. Inorganic nanosheets like graphene, graphitic boron nitride, 2D transition metal dichalcogenides, layered metal oxides, layered double hydroxides, and some clays and silicates are extensively studied for their charge and heat transport properties,[2] as well as their capacity to form stacked architectures.[3] Naturally occurring 2D biological nanomaterials, like cell membranes and S-layer proteins, are also well studied and play a central role in biology. Synthetic, organic 2D nanomaterials are far less common, and are now receiving increased attention because of their great promise as components in a variety of nanotechnologies such as filtration, chemical sensing, catalysis, and photovoltaics.[4−6] Because of the growing interest in the diverse properties of organic 2D nanomaterials, there is a pressing need for efficient and general synthetic routes to make and engineer this class of material. Of particular importance for biomedical applications are synthetic approaches to produce large quantities of free-floating 2D nanomaterials that are biocompatible and can be highly functionalized.

There are presently three main approaches for the synthesis of organic 2D nanomaterials:[4] the exfoliation/cleavage of lamellar crystals, the supramolecular assembly and/or polymerization of molecular building blocks in solution, and the adsorption of building blocks to an interface. The exfoliation[1,7−10] and micromechanical cleavage of crystals,[11] the most common method for inorganic 2D nanomaterial synthesis,

* Address correspondence to rnzuckermann@lbl.gov.

Received for review September 5, 2014 and accepted October 19, 2014.

Published online October 19, 2014
10.1021/nn505007u

has great potential to produce single-crystal two-dimensional polymers on a large scale. The technique also has synthetic limitations, in that it requires materials that form lamellar crystals, the size of the material is limited by the size of the crystal, the exfoliated sheets can reaggregate, and the chemical structure cannot be readily fine-tuned. The direct synthesis of organic 2D nanomaterials from solution overcomes some of these limitations, and several elegant approaches have been recently reported.[4,8,12−14] This approach typically uses rigid, symmetric, small-molecule building blocks bearing multiple reactive groups that can combine to form 2D periodic networks bound covalently or noncovalently. This provides a flexible route to surface-functionalized 2D nanomaterials. However, most of the materials in this class are produced in organic solvents and are not readily biocompatible. A third approach to the synthesis of organic 2D nanomaterials is to use the inherent planarity of interfaces to direct the assembly of building blocks.[15] Molecular[16−22] and nanoparticle[23] units can be designed to adsorb to this planar interface, and once aggregated, multiple attractive interactions between the molecules result in supramolecular self-assembly, which can be followed by polymerization and/or cross-linking. The planarity and molecular orientation of the assembly so produced can persist even when desorbed from the interface, producing an ultrathin 2D material. This strategy is well suited for producing small quantities of material, for example as a surface coating, but it is less suited to producing free-floating 2D nanomaterials in large quantities, because release of the nanosheet from the surface can be very slow. Thus, there remains a critical need for high-yielding, general, scalable and direct synthetic routes to highly functionalized, biocompatible nanosheet materials.

We recently discovered a powerful new route to 2D nanomaterials, based on the hierarchical supramolecular assembly of peptoid polymers at an air−water[24] or oil−water interface.[25] The approach relies on the chemical synthesis of sequence-defined amphiphilic peptoid polymer chains that assemble into a monolayer at an air−water interface. Peptoids are a highly designable,[26] biologically active,[27,28] and efficiently synthesized[29,30] class of bioinspired polymer, with N-substituted side chains appended from a glycine backbone.[31−38] Relative to C_α-substituted peptides, *N*-substitution in peptoids eliminates backbone chirality and backbone hydrogen bonding, facilitating extended planar configurations stabilized by multiple weak interactions.[24,39,40] At the air−water interface, peptoids containing an alternating sequence of polar and nonpolar monomers organize into a monolayer *via* adsorption from solution. Under compression, the monolayer collapses into a bilayer and desorbs from the air−water interface. During collapse, the two hydrophobic faces contact each other and physically bind to irreversibly form free-floating bilayer nanosheets. Under decompression, polymer chains from solution repopulate the interface, forming a new monolayer in equilibrium with the reservoir of polymers dissolved in the water phase.[24]

The nanosheets formed through this approach are ordered, solid bilayers with a hydrophobic core and a polar, zwitterionic surface, and have macroscopic lateral dimensions (up to hundreds of microns) and nanoscopic thickness (~3 nm).[24,39,40] The nanosheet-forming peptoid sequence motif is surprisingly tolerant to substitution, raising the possibility of convenient access to a broad new class of highly functionalized 2D nanomaterials.[41] Functional domains as long as 33% of the length of polymer can be inserted into a sheet-forming sequence, and form a folded, supramolecular nanosheet with surface-displayed loop domains.[41] Importantly, peptoid nanosheets are extremely stable and maintain their structure even at elevated temperatures and in the absence of water.[40] These properties make peptoid nanosheets a promising platform for a wide variety of problems in materials science, sensing and diagnostics, separation science and protein mimicry.

The monolayer compression production cycle can be repeated hundreds of times until most of the peptoid chains are converted to nanosheets. Assembly at an air−water interface therefore offers a distinct advantage over assembly at a solid interface: the air−water interface can be regenerated, and therefore act as a catalyst. Each monolayer compression cycle has a characteristic surface pressure/area trace that can be measured using a Langmuir trough. The surface (interface) pressure increases with compression until the monolayer collapses, which coincides with a distinct reduction in slope and the emergence of significant hysteresis in the area-pressure isotherm (Figure 1d). The production of nanosheets scales linearly with the number of surface compressions (at a given solution peptoid concentration), provided that the compression ratio is high enough to cause collapse.[24] The nanosheet formation mechanism is notably distinct from the compression and collapse of lipid monolayers, where low stabilities give rise to multilayers or vesicles.[42,43] Free-floating lipid bilayers (bicelles) can only be produced in low yield *via* careful desorption of bilayers from a solid interface.[44]

Here we further characterize the peptoid nanosheet monolayer compression mechanism, and determine at which stages of assembly the nanoscale and atomic-scale ordering appear. We use X-ray scattering, grazing incidence X-ray scattering at the air−water interface, electron diffraction, and a recently developed computational coarse-grained peptoid model[45] to probe the molecular ordering at various stages of assembly. We found that the lateral packing and organization of the chains is determined during the monolayer formation stage, prior to the monolayer's collapse into a bilayer. Identifying the structure-determining step suggests

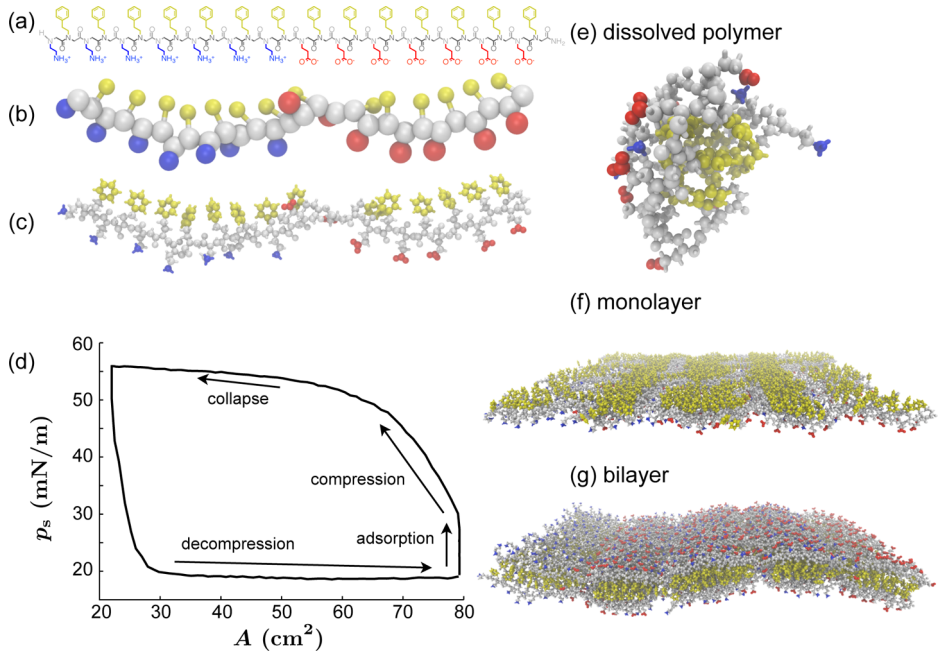

Figure 1. (a) Chemical structure of the block-28 peptoid, illustrating the block pattern of charges (positive *N*-2-aminoethyl and negative *N*-2-carboxyl groups are blue and red, respectively) and the apposed hydrophobic portion of the molecule (*N*-2-phenylethyl groups are yellow). (b and c) Ball-and-stick representation of (b) the coarse-grained sites and (c) the estimated atomic positions for a peptoid equilibrated in a nanosheet. (d) Experimental compression isotherm of the nanosheet production cycle. Under contraction of the interface, the monolayer first reversibly compresses, then irreversibly collapses, producing bilayer nanosheets. Decompression leads to an under-saturated monolayer, which equilibrates over time (450 s shown here) as peptoids adsorb. (e–g) Simulation snapshots of (e) a single dilute block-28 peptoid dissolved in water, (f) an equilibrated monolayer, and (g) a bilayer nanosheet. Subsequent figures show the molecular-scale features of (f) and (g).

new strategies for influencing nanosheet order by thermal annealing of the monolayer intermediate, and for predicting production yields based on the monolayer compression behavior. This understanding enables the engineering of atomic-scale structural features into supramolecular nanosheets, through the rational design of the component molecular building blocks.[46−49] Introducing protein-like functions, like specific molecular recognition and catalysis, will require control over the precise orientation of multiple functional groups within the nanomaterial. The ability to create highly ordered and chemically diverse 2D nanomaterials of mesoscopic dimension will enable a host of high-surface area functional materials, which will find broad application.

RESULTS AND DISCUSSION

In this study, we focus on a previously reported single peptoid 28mer sequence that produces nanosheets in high yield.[41] The peptoid sequence is composed of three monomers, *N*-(2-aminoethyl)glycine (Nae), *N*-(2-phenylethyl)glycine (Npe), and *N*-(2-carboxyethyl)-glycine (Nce). The sequence is designed with alternating hydrophobic (Npe) and hydrophilic monomers, where the hydrophilic units are positively (Nae) and negatively (Nce) charged in contiguous blocks ([Nae-Npe]$_9$-[Nce-Npe]$_9$; see chemical structure in Figure 1a). We refer to this peptoid as block-28, because it is 28 monomer units long and its charge types are arranged in two blocks. We find that the structure, interfacial adsorption and collapse behavior of the single-chain block peptoids[25,39,41] are similar to those of related binary systems[24,40] composed of two separate positively and negatively charged strands. We therefore expect that nanoscale insight into the ordering mechanism of the block-28 peptoid should be applicable to amphiphilic nanosheet-forming peptoids generally. In what follows, we describe our use of X-ray scattering, electron microscopy, and computational modeling to determine at which stages of the assembly process the molecular structure of the nanosheets appears.

To determine the in-plane structure of the peptoid monolayer, we performed grazing-incidence X-ray scattering (GIXS) (Figure 2a) on an equilibrated monolayer in a Langmuir trough, at section 9ID of the Advanced Photon Source of Argonne National Laboratory. We found a peak at 1.3 Å^{-1}, corresponding to lateral structures correlated on a length scale of 4.7 Å (Figure 2b). Upon compression of the trough by an area reduction of 16%, the location of the peak remained constant to within 0.1 Å (see Supporting Information Figure S1). This suggests that the peptoid chains have a well-defined structure over a range of surface pressures: compression modulates the fraction of the monolayer in the structured phase, rather than uniformly compressing the nanostructure. We tested this expectation by combining our structural and

thermodynamic measurements with real-space computational modeling.

To efficiently model the monolayer and bilayer over a range of thermodynamic conditions, we recently created a coarse-grained molecular peptoid model consisting of two oriented sites per monomer.[45] We parametrized the model to match available experimental data for nanosheets, monolayers, and dissolved peptoids (Figure 1e–g), while also matching detailed structural data obtained with all-atom simulations of nanosheets. Incorporating orientated coarse-grained sites allowed us to implicitly account for atomic scale interactions and estimate the locations of all the atoms in the peptoids (Figure 1c), which we used to create snapshots (Figure 1e–g) and simulated X-ray scattering spectra.

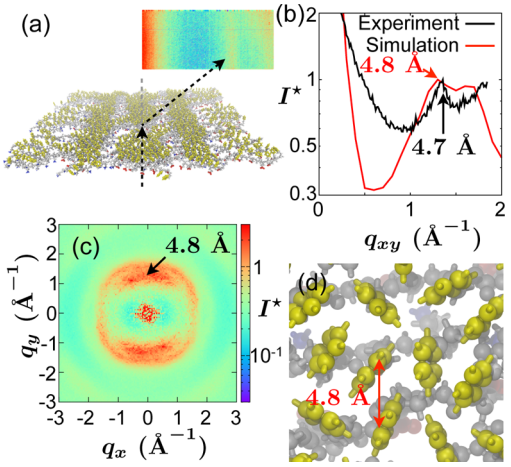

Figure 2. (a and b) Grazing-incidence X-ray scattering spectra of a peptoid monolayer from experiment (black) and simulation (red) show that a 4.7 Å peak (4.8 Å in the simulation) is a feature of the in-plane monolayer structure. (c) Two-dimensional in-plane spectrum of the anisotropic simulation sample and (d) snapshots of simulated monolayers reveal that this peak results from the characteristic spacing between parallel peptoid polymers.

Calculating a simulated X-ray spectrum for a monolayer at the experimental equilibrium surface pressure, we find a dominant peak with a similar location as the experimentally observed peak at 4.7 Å (Figure 2b). One feature of the simulated X-ray scattering is the radially anisotropic simulation sample: the polymers remain oriented along the x direction across the periodic simulation box. This allows us to resolve the X-ray scattering into parallel (*x*) and perpendicular (*y*) components (Figure 2c). Comparison with simulation snapshots (Figure 2d) confirms that the dominant peak corresponds to the typical spacing between parallel polymer chains.

To understand why the experimental peak location did not shift with compression of the monolayer, we carried out monolayer simulations at several fixed pressures over a broad range, with no peptoids present in the (implicit) water volume (Figure 3). At zero surface pressure, the monolayer fully melted in the direction perpendicular to the peptoid backbones, resulting in a concentrated phase coexisting with a dilute phase (Figure 3a). Comparing the simulated X-ray spectra (Figure 3d) and close-up snapshots (Figure 3e–f) for a variety of surface pressures reveals that, while the concentration is very sensitive to surface pressure, the local molecular structure, or chain ordering, within the concentrated phase is not. The tendency for peptoids

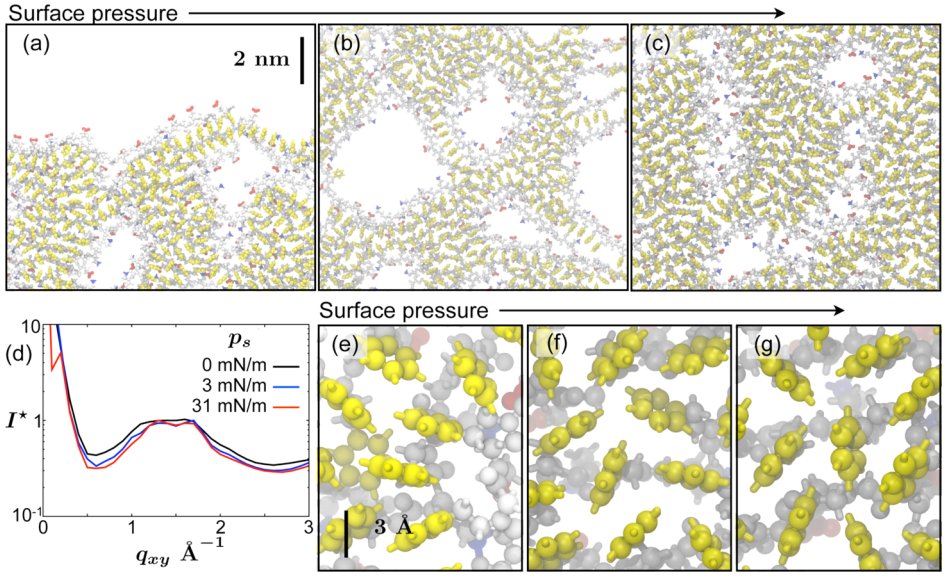

Figure 3. (a–c) Snapshots of simulated peptoid configurations at three different surface pressures: 0, 3, and 31 mN/m, with corresponding surface concentrations of 1.7, 4.0, and 5.8 residues/nm^2. (d) Simulated X-ray spectra at the three pressures show that, while the average surface concentration varies strongly with surface pressure, the local chain ordering within the concentrated phase does not. (e–g) Zoomed-in snapshots illustrate that the packing and local chain ordering within the concentrated phase at the three different surface pressures are comparable.

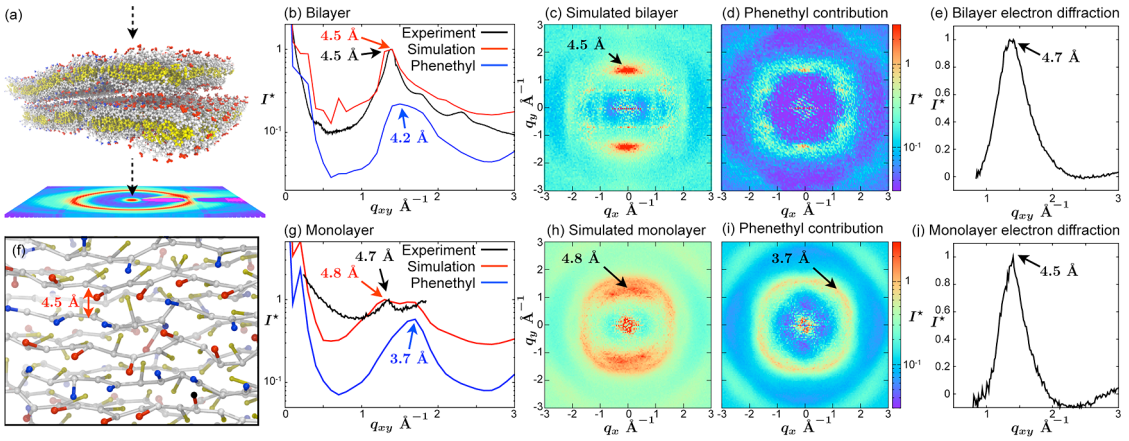

Figure 4. (a) Schematic showing the geometry of the in-plane X-ray scattering, using the simulated stack of bilayers for illustration. (b) In-plane bilayer X-ray scattering spectra from experiment (black) and simulation (red) show a dominant peak at 4.5 Å. The contribution from the *N*-2-phenylethyl side chain in simulation (blue curve) reaches a maximum nearby. (c) Two-dimensional in-plane spectrum of the radially anisotropic simulated bilayer confirms that the dominant in-plane peak comes from the characteristic separation between parallel peptoids. (d) The 2-phenylethyl contribution shows a preference for particular directions. (e) Electron diffraction measurement of a single nanosheet bilayer. (f) Snapshot of the simulated bilayer shows a rectilinear configuration characterized by a typical separation of 4.5 Å between parallel polymers. (g) For comparison, the X-ray scattering peak for the monolayer is less sharp, in part due to a competing contribution from the 2-phenylethyl side chains at 3.7 Å. (h and i) The mild peak at 3.7 Å in simulations is due to a largely isotropic contribution from 2-phenylethyl side chains. (j) Electron diffraction measurement of a single peptoid monolayer.

to cluster into a locally structured state explains the insensitivity of the experimental X-ray peak location to surface pressure. Clustering also suggests a mechanism for rapid adsorption and ordering at the air−water interface: during adsorption, clustering hastens the formation of local structure and opens up large voids available for further adsorption.

Comparing the experimental X-ray and electron diffraction data of the monolayer and bilayer nanosheets reveals a strong similarity between their structural features. By drying a solution of nanosheets on a Kapton grid (see experimental section), we were able to create an oriented stack of nanosheets for X-ray scattering relative to a preferred direction (Figure 4a). We found that the in-plane scattering spectrum (Figure 4b) exhibits a peak at 4.5 Å, similar to the monolayer's peak at 4.7 Å (Figure 4g). We independently verified this comparison of in-plane structure by performing electron diffraction on a single nanosheet and a single monolayer, again obtaining similarly located peaks at 4.7 and 4.5 Å, respectively (Figure 4e,j). As for the monolayer, comparing simulation snapshots (Figure 4f) with two-dimensional simulated X-ray spectra (Figure 4c) indicates that the bilayer's dominant peak corresponds to the typical spacing between parallel, extended polymers. Since the monolayer is a precursor to the nanosheet, this suggests that the arrangement of polymers within each leaflet of the nanosheet is determined by their arrangement in the monolayer.

Closer comparison between the bilayer (Figure 4b) and monolayer (Figure 4g) X-ray spectra reveals subtle differences in their structure. The bilayer's dominant peak is sharper, and the experimental monolayer appears to have a second peak at 1.7−1.8 Å^{-1}, consistent with a second peak found in the simulated monolayer. Decomposing the simulated X-ray spectrum into components reveals that this second peak is due to correlations between the 2-phenylethyl side chains (blue curve in Figure 4g). These competing correlations are largely isotropic, as illustrated by the ring in the two-dimensional simulated X-ray spectra of the entire monolayer (Figure 4h) and the phenethyl side chains in the monolayer (Figure 4i). In contrast, phenethyl correlations in the bilayer (Figure 4d and blue curve of Figure 4b) occur at a spacing closer to the polymer spacing and are more anisotropic, showing distinct preferences for certain directions in the x−y plane. This anisotropy mirrors the total two-dimensional bilayer spectrum (Figure 4c), which exhibits a weak peak at 3.0 Å in the x direction, corresponding to the spacing between residues, and an off-axis peak corresponding to approximately rectangular symmetry, similar to weak peaks observed in both stacked[50] and monolayer[51] β-sheet structures. These observations suggest that there is liquid-like order in the aromatic region of the monolayer that converts to more crystalline order in the nanosheets. The liquid-like order may aid assembly in that it may allow rearrangement of the side chains during collapse into the more directional order found in the bilayer. The opposing leaf of a collapsing monolayer may ultimately assist in further structuring of its aromatic face by presenting an interface that is more structured than air.

Taken together, our X-ray scattering, electron diffraction, and computational modeling indicate that nanosheet assembly is facilitated by preordering within the monolayer: the equilibrated monolayer has similar *in-plane* structure to the bilayer nanosheet, allowing efficient collapse into a nanosheet with

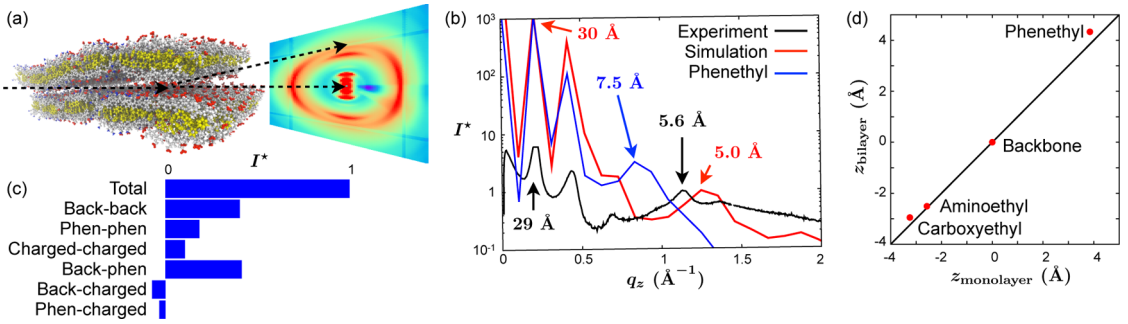

Figure 5. (a) Schematic showing the geometry of the transverse X-ray scattering, using the simulated stack of bilayers for illustration. (b) Out-of-plane bilayer spectrum shows that the 29 Å sheet-stacking peak (30 Å in the simulation) and the 5.6 Å short-range peak (5.0 Å in the simulation) are features of the bilayer's out-of-plane structure. The sheet-stacking peak is stronger in the simulation because of the perfect periodicity of the two-bilayer periodic cell. (c) Decomposing contributions to the 5.0 Å transverse peak in the simulation by correlations between regions within the peptoids (backbone, phenethyl side chains, and charged side chains) reveals that the peak arises from a nontrivial addition of many contributions. (d) The average heights of coarse-grained sites in the simulation agree when comparing the monolayer (*x* axis) and individual leaves of the bilayer (*y* axis), as long as the heights flipped appropriately to account for the orientation of each bilayer leaf. Heights are plotted relative to the average backbone height, and the diagonal represents perfect agreement. The bilayer shows a somewhat smaller range, indicating that it is somewhat more compact in the vertical direction.

relatively little reorganization within each leaf. Ideally, we would also experimentally compare the *out-of-plane* structure of monolayers and nanosheets. However, we have not been able to find a suitable experimental technique that can probe the out-of-plane structure of both monolayers and bilayers. Instead, we have developed separate experimental techniques for monolayers and bilayers, compared results from those techniques with our simulations, and used the simulations to directly compare monolayer and bilayer out-of-plane structure.

Recently, vibrational sum frequency (VSF) spectroscopy was used to reveal information about the orientation of atomic bonds in monolayers of the block-28 peptoid at an oil–water interface.[25] It was shown that several side chain groups have a net orientation relative to the interface normal. For instance, the VSF spectrum showed a sharp peak at a wavelength corresponding to the five CH bonds surrounding the aromatic ring of the *N*-2-phenylethyl side chain. This indicates that the phenyl groups have a strong net orientation relative to the interface. This measurement is consistent with our simulations, where the distribution of phenyl angles are also oriented, with mean and standard deviation angles of 48 ± 27°.

We were able to extract detailed out-of-plane structural information for nanosheets by performing X-ray scattering with the incident beam oriented "edge-on" to dried stacks of nanosheets and recording scattered X-rays in the transverse direction (Figure 5a,b). The strong peak at 0.22 Å^{-1} indicates that sheets are stacked with a period of 29 Å, consistent with nanosheet thicknesses independently measured with atomic force microscopy.[40] The intensity of this peak, together with the absence of any peak at 4.5 Å associated with the in-plane spacing of parallel peptoids, supports the idea that the nanosheets stack flat against the Kapton grid during sample preparation, during either the evaporation step or the centrifugation step.[52] The subsequent peak at twice this wavenumber is possibly a combination of two contributions: the second harmonic of the 29 Å peak, and additional periodic structures repeating approximately twice per sheet, such as the location of the polymer backbones in each leaf of the bilayer. Finally, the peak at 5.6 Å suggests that the nanosheets have short-range structure in the transverse direction.

When we originally found the 5.6 Å peak in isotropic powder X-ray scattering spectra, we ascribed it to correlations across leaflets between the aromatic groups in the nonpolar side chains.[40] Although our simulations exhibit a peak at 5.4 Å for the radial distribution function of 2-phenylethyl side chain sites, decomposing the simulated X-ray spectrum into contributions from different molecular groups indicates that this spacing is not on its own responsible for the transverse X-ray peak: when we calculated spectra from simulations by including diffraction contributions *only* from atoms in the phenethyl side chains, we found a peak at 7.5 Å (blue curve in Figure 4b). The overall peak at 5.0 Å is instead a subtle combination of many contributions, with backbone–backbone and backbone–phenethyl contributions outweighing the contribution from phenethyl–phenethyl correlations (Figure 4c).

We can use our simulations to compare the out-of-plane structure of monolayers and of individual leaves of bilayer nanosheets. Figure 4d shows a scatter plot of average out-of-plane heights of the coarse-grained sites (relative to the backbone sites), where the *x*-axis denotes the average height in the monolayer and the *y*-axis denotes the average height in the bilayer leaf (multiplying top leaf positions by −1 so that the nonpolar side is always "up"). The predominance of data points along the diagonal indicates that the out-of-plane structure of monolayers and bilayers is similar. Together with our experimental and computational

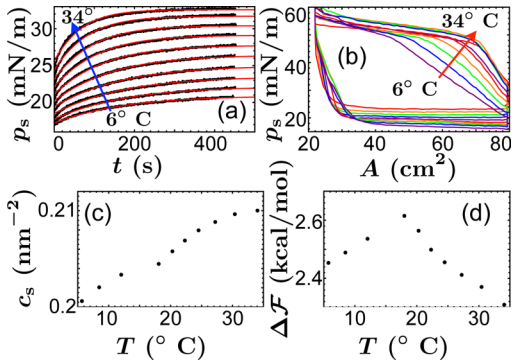

Figure 6. (a) Experimental time-dependent surface adsorption (dense black data points) shows faster adsorption at higher temperatures. This allows for a faster nanosheet production cycle. Our diffusion-adsorption model (smooth red curves in (a)) reproduces the experimental adsorption curves. (b) Higher temperatures also result in a larger range of area over which collapse occurs (top horizontal region). (c and d) Temperature dependence of the model fit parameters shows that the equilibrium surface concentration (c_s) increases slightly with temperature, while the free energy barrier for adsorption (ΔF) decreases with temperature.

analysis of the in-plane structure, these results indicate that the monolayer possesses much of the structure necessary to form a bilayer nanosheet: forming a bilayer nanosheet may require little structural change *within* the portions of the monolayer that become leaflets of the nanosheet. However, the dynamics of the structural change *between* monomers is still largely unknown. Under compression, monolayers must select a leading edge for collapse, break into two leaves that flip relative to each other, and then arrange their *relative* in-plane orientation and position as the leaves physically bind. Further experiments and simulations are needed to shed light on this complex process.

Since the chain ordering of the nanosheets is determined in large part in the monolayer, a promising strategy to improve the quality and yield of nanosheets is to influence the quality and yield of the monolayer. We hypothesized that to increase structural order in the nanosheets, we can increase the temperature during adsorption, allowing the monolayer to better escape kinetic traps.[53] Additionally, if the rate-limiting step for nanosheet formation is monolayer formation, then increased temperature could also increase nanosheet production rates, since the rate of adsorption of related oligomers has been shown to increase with temperature.[54]

We tested this hypothesis by producing nanosheets at higher temperatures. The peptoid solution was slowly heated and cooled over the course of many Langmuir trough production cycles, each allowing 450 s for adsorption followed by compression of the interface area linearly by 72% over 33 s. Adsorption occurred faster at higher temperature, as indicated by the faster rise in surface pressure at higher adsorption temperature (Figure 6a). We were able to model the temperature- and time-dependent rise in surface pressure with a simple analytic model for the diffusion of dissolved peptoids, activated adsorption onto the interface, and saturation of the monolayer (see Supporting Information Figure S2). Because we could not measure the surface concentration experimentally, we used coarse-grained model simulations to convert surface concentration to surface pressure. The two fit parameters of the analytic model are the magnitude of the energy barrier and the maximum saturated surface concentration at the interface.

The fit parameters reveal trends in surface adsorption as a function of temperature. At higher temperatures the saturated molecular density at the interface is slightly larger than at lower temperature, while the energy barrier is slightly smaller (Figure 6c,d). The consequence of these differences is that, given a nanosheet production cycle with a fixed waiting time between compressions, more molecules will be found at the air−water interface, so a lower compression ratio will be required for collapse.

This effect is clearly seen in the experimental isotherms of Figure 6b. The isotherms reveal that monolayer collapse occurs at approximately the same surface pressure for all three temperatures, which does not by itself suggest any structural improvement in the monolayer. However, the compression ratio required for collapse decreases dramatically at the higher temperatures. For example, at 6 °C collapse occurs at a compression ratio of 1.96, at 18 °C collapse occurs at a compression ratio of 1.3, and at 42 °C it occurs at a ratio of 1.1. Compression beyond the collapse pressure continues to produce further monolayer collapse events. As collapse corresponds to nanosheet production, this would suggest that at higher temperatures we would produce more nanosheets per compression. (Alternatively, producing the same quantity of nanosheets at low temperature would require longer adsorption waiting times.)

Motivated by this prediction, we measured the dependence of nanosheet yield on temperature in experiment by producing nanosheets by vial rotation[24] at three different temperatures (19, 40, 60 °C), with three different monolayer adsorption pauses (30, 100, 450 s), for 3 h of production. The relative quantities of nanosheets in each solution were measured with a solvatochromatic fluorescence assay using Nile Red dye. Across these nine systems, we found that increasing temperature increased the overall nanosheet yield, consistent with our prediction (see Supporting Information section S3). Decreasing the waiting time for adsorption also increased the overall yield observed after 3 h of repeated compression and adsorption cycles, indicating that the gain in yield from further adsorption does not compensate the time lost by pausing longer than 30 s.

To probe the stability of nanosheets produced at higher temperatures and shorter adsorption times, we

compared nanosheets produced at 60 °C (with a 30 s. adsorption time) to those produced at 19 °C (with a 450 s. adsorption time). To evaluate stability, we measured the nanosheet's resistance to electron beam damage, by monitoring the decay of the electron diffraction pattern under electron irradiation.[55] Electron diffraction patterns of each nanosheet were gathered at increasing cumulative exposures to 200 keV electrons. The full-width half-maxima of the 4.6 Å peaks broadened with cumulative exposure, but the 60 °C nanosheets exhibited dramatically greater resiliency to beam-damage (see Supporting Information Figure S3). This indicates that monolayer annealing may be an effective strategy to produce nanosheets of increased molecular order.

CONCLUSION

We have shown that key features of the local molecular structure of peptoid nanosheets are determined largely during monolayer formation. The in-plane structure, as measured by X-ray scattering and electron diffraction, appears similar in the monolayer intermediate and in the resultant bilayer nanosheets. Simulations using a coarse-grained peptoid model reveal that the dominant peak from these Fourier space measurements correspond to the real-space separation between adjacent, extended peptoid chains. Although these simulations also suggest that the out-of-plane structure is similar in monolayers and individual bilayer leaves, direct experimental measurement of structure in this nanoscopically thin direction is difficult. We also found that monolayer formation from subphase adsorption of the peptoid to the air–water interface is the rate-limiting step to nanosheet production under a broad range of thermal and temporal conditions. Increasing temperature increased the rate of formation of the monolayer. A simple diffusion-adsorption model suggests that this is due to a combination of faster diffusion and lower adsorption energy barriers.

Our results suggest new strategies for introducing structural modifications into nanosheets. Building blocks must be designed so that the adsorbed monolayer and the target bilayer have commensurate structure. Since chain ordering within the nanosheet is largely determined in the monolayer, structural modifications such as photoswitching,[56] photo-cross-linking,[17,18] ligand binding,[20] and interfacial reactions with the gas phase[57] may be conveniently performed at the air–water interface. It is expected that the recently reported assembly of peptoid nanosheets at the oil–water interface[25] follow a similar mechanism. It also points to limits on the degree of chemical modification possible to the peptoid structure, since the chain's overall monolayer adsorption properties must be maintained.[41] Nonetheless, a huge diversity of functionalized nanosheets can be produced using the monolayer collapse mechanism, and these new materials, as a class, hold promise for many potential applications. More generally, our results provide insight into the general strategy of utilizing planar fluid interfaces to catalytically assemble 2D nanomaterials.

MATERIALS AND METHODS

X-ray Analysis at the Air–Water Interface. GIXS and reflectometry data were gathered at beamline ID-9C at the Advanced Photon Source (APS) at Argonne National Laboratory. A 20 μM Block-28 peptoid solution was placed in an enclosed Langmuir trough in a helium atmosphere (0.3% Oxygen). As shown in the surface pressure *vs* bulk concentration curve of Supporting Information Figure S4, this concentration results in a moderately saturated monolayer. X-rays (0.92 Å) were incident to the surface, while a line charge coupled device (CCD) was used to measure scattering, and a photomultiplier tube was used for reflectometry measurements. The X-ray incidence and detection angles were computer controlled, as were the position of the sample and the helium-exposed surface area of the trough. Reflectometry measurements confirmed that we had a monolayer: a three-step electron density model fit the reflectometry data with a 11.5 Å thick layer showing 35% greater electron density than water, followed by two thinner layers of total thickness 9.3 Å showing 2–4% greater electron density than water.

Oriented X-ray Scattering. X-ray diffraction data were collected at a multiple-wavelength anomalous diffraction and monochromatic macromolecular crystallography beamline, 8.3.1, at the Advanced Light Source located at Lawrence Berkeley National Laboratory. Beamline 8.3.1 has a 5 T single pole superbend source with an energy range of 5–17 keV. Data were collected with a 3 × 3 CCD array (ADSC Q315r) detector at a wavelength of 1.1159 Å. Data sets were collected with the detector 200 mm from the sample. The peptoid sheet solutions were concentrated approximately 100-fold in an Amicon Ultra centrifugal filter (100 kDa MWCO, Millipore) then centrifuged at 13 200 rpm for 20 min. After removing the supernatant, the resulting peptoid sheet pellet was pipetted onto a Kapton mesh (MiTeGen). Data was processed with custom Matlab (Mathworks) scripts.

Electron Microscopy. The monolayer sample was created by submerging a plasma-etched, continuous carbon EM grid beneath the surface of a peptoid solution in a Langmuir trough, immediately after the surface was aspirated. The monolayer was then formed at the air–water interface over the subsequent 1800 s. The grid was pulled at 0.4 mm/sec. This is an adapted Langmuir–Blodgett approach[15] which we have previously used to show monolayer peptoid deposition by atomic force microscopy.[24] The nanosheet sample was created by depositing a 5 μL droplet of nanosheet solution onto a lacey-carbon EM grid and gently centrifuging it at 320 rpm for 15 min before removing the excess liquid with filter paper. Electron diffraction patterns samples were gathered with a Libra 200MC at the National Center for Electron Microscopy.

Peptoid Nanosheet Production by Vial Rotation. Pure, lyophilized peptoid was dissolved in a 2:1 (v/v) mixture of DMSO/water to obtain a 2 mM peptoid stock solution stored at room temperature. In a clean, cylindrical 4 mL glass vial, 500 μL of nanosheet-forming solution (20 μM peptoid, 10 mM buffer) in Milli-Q water was prepared from the 2 mM peptoid stock solution. Nanosheets were prepared by rotating a partially filled vial of peptoid solution in 2-amino-2-methyl-1,3-propandiol (AMPD), pH 9.0 buffer as previously described.[24]

Relative Peptoid Nanosheet Production Measured by Fluorescence. Solutions with nanosheets were placed in multiwell plates with 2 μM Nile Red, a solvatochromatic dye. Wells were excited with

590 nm light, and emission was observed from 600 to 700 nm. A nanosheets solution produced by vial rotation to completion and an undisturbed but similarly aged vial of peptoids served as reference spectra, and demonstrated a significant shift in the Nile Red's fluorescence intensity and peak position between the reference samples. The difference in the amount nanosheets in solution was qualitatively confirmed by differential interference contrast imaging. Relative nanosheet production was measured by fitting the spectrum of solutions that had been producing nanosheets for a relatively short while (3 h) to a linear combination of the nanosheet-rich and nanosheet-poor reference spectra.

Langmuir Trough. The Langmuir trough (Mini-trough, KSV Nima, Finland) was equipped with an inverted microscopy attachment and paper Wilhelmy plates. The solutions were mixed in the trough with gentle pipet action prior to compressions. Unless otherwise noted, the wait time between compressions was 450 s, and the compression rate was 100 cm^2/min.

Coarse-Grained Peptoid Model. We defined, parametrized, and simulated the coarse-grained model as discussed elsewhere.[45] Each block-28 peptoid is represented by a chain of 28 backbone sites, each bonded to one side chain site. We characterize each site by a position and a principle symmetry direction. For the backbone site, the position maps to the backbone nitrogen position and the direction maps to the N−C_β bond. For the phenethyl side chain site, the position maps to the center of the aromatic ring and the direction maps to the ring normal. For the aminoethyl and carboxyethyl side chain sites, the position maps to the center of mass and the direction maps to the C−N and the last C−C bond, respectively. The potential energy function is a sum of terms: pairwise nonbonded terms between bonded sites, pairwise bonded terms between bonded side chain and backbone sites, three-body terms between three successive backbone bonds, and (in the case of the monolayer) solvation terms that depend on the height of sites relative to a static air−water interface. The nonbonded and bonded terms depend on both position and orientation. The functional forms and parameters for all terms are published elsewhere.[45]

We modeled small pieces of monolayers and bilayers in equilibrium by performing periodic Metropolis Monte Carlo simulations[58] in a rectilinear periodic box at fixed number, water volume, temperature, and in-plane pressure, arranging the monolayers and bilayers normal to the *z* axis so that they wrapped around the periodic boundary conditions in the x and y direction. We allowed the periodic box and all coordinates within it to affinely fluctuate shape under the constraint that the total water volume (total box volume in the case of the bilayer) remained constant. For the bilayer, we set the in-plane pressure equal to 0, mimicking a small piece of a free-floating bilayer under zero tension. For the monolayer, we varied the surface pressure between 0 and 72 mN/m, the value that would neutralize the surface tension of water. Note that we did not allow fluctuations in the location of the air−water interface, so the surface tension was not a parameter of our simulations. We initialized our simulations in low-energy configurations and allowed them to equilibrate before recording data. We used monolayers with 48 peptoids (2 in the long direction and 24 in the perpendicular) and bilayers with 96 peptoids (two leaves, each 2 × 24).

We estimated the location of all the atoms by combining the positions and orientations of the coarse-grained sites with knowledge of the preferred local chemistry near each site. We calculated the X-ray scattering spectra *via*

$$I(\mathrm{q}) = |\sum_j f_j \exp(-\vec{\mathrm{q}} \cdot \vec{\mathrm{r}}_j)|^2$$

where the sum runs over all atoms. We set the atomic scattering factor f_j equal to the atomic number, since this is nearly exact for the experimental 11 keV X-rays.[59]

Conflict of Interest: The authors declare no competing financial interest.

Supporting Information Available: Grazing-incidence X-ray spectra of block-28 peptoid monolayers under compression; analytic model of monolayer formation; dependence of nanosheet yield on temperature and wait-time; nanosheet resilience to electron beam damage; surface pressure *vs* concentration. This material is available free of charge *via* the Internet at http://pubs.acs.org.

Acknowledgment. This project was funded by the Defense Threat Reduction Agency under Contract No. IACRO-B1144571. The work was conducted at the Molecular Foundry with support from the Advanced Light Source and the National Energy Research Scientific Computing Center, at Lawrence Berkeley National Laboratory, all of which are supported by the Office of Science, Office of Basic Energy Sciences, U.S. Department of Energy, under Contract No. DE-AC02-05CH11231. Experiments performed at the Advanced Photon Source at Argonne National Laboratory was supported by the U.S. Department of Energy, Office of Science, Office of Basic Energy Sciences, under Contract No. DE-AC02-06CH11357. We also thank I. Kuzmenko (Argonne beamline), J. Holton (ALS beamline) and C. Kisielowski (electron microscopy).

REFERENCES AND NOTES

1. Nicolosi, V.; Chhowalla, M.; Kanatzidis, M. G.; Strano, M. S.; Coleman, J. N. Liquid Exfoliation of Layered Materials. *Science* **2013**, *340*, 1226419.
2. Butler, S. Z.; Hollen, S. M.; Cao, L.; Cui, Y.; Gupta, J. A.; Gutierrez, H. R.; Heinz, T. F.; Hong, S. S.; Huang, J.; Ismach, A. F. Progress, Challenges, and Opportunities in Two-Dimensional Materials Beyond Graphene. *ACS Nano* **2013**, *7*, 2898.
3. Govindaraju, T.; Avinash, M. Two-Dimensional Nanoarchitectonics: Organic and Hybrid Materials. *Nanoscale* **2012**, *4*, 6102–6117.
4. Colson, J. W.; Dichtel, W. R. Rationally Synthesized Two-Dimensional Polymers. *Nat. Chem.* **2013**, *5*, 453–465.
5. Sakamoto, J.; van Heijst, J.; Lukin, O.; Schlüter, A. D. Two Dimensional Polymers: Just a Dream of Synthetic Chemists? *Angew. Chem., Int. Ed.* **2009**, *48*, 1030–1069.
6. Tanoue, R.; Higuchi, R.; Enoki, N.; Miyasato, Y.; Uemura, S.; Kimizuka, N.; Stieg, A. Z.; Gimzewski, J. K.; Kunitake, M. Thermodynamically Controlled Self-Assembly of Covalent Nanoarchitectures in Aqueous Solution. *ACS Nano* **2011**, *5*, 3923–3929.
7. Gallego, A.; Hermosa, C.; Castillo, O.; Berlanga, I.; Gómez-García, C. J.; Mateo-Martí, E.; Martínez, J. I.; Flores, F.; Gómez-Navarro, C.; Gómez-Herrero, J.; Delgado, S.; Zamora, F. Solvent-Induced Delamination of a Multifunctional Two Dimensional Coordination Polymer. *Adv. Mater.* **2013**, *25*, 2141–2146.
8. Bhola, R.; Payamyar, P.; Murray, D. J.; Kumar, B.; Teator, A. J.; Schmidt, M. U.; Hammer, S. M.; Saha, A.; Sakamoto, J.; Schlüter, A. D.; King, B. T. A Two-Dimensional Polymer from the Anthracene Dimer and Triptycene Motifs. *J. Am. Chem. Soc.* **2013**, *135*, 14134–14141.
9. Kissel, P.; Murray, D. J.; Wulftange, W. J.; Catalano, V. J.; King, B. T. A Nanoporous Two-Dimensional Polymer by Single-Crystal-to-Single-Crystal Photopolymerization. *Nat. Chem.* **2014**, *6*, 774–778.
10. Kory, M. J.; Wörle, M.; Weber, T.; Payamyar, P.; van de PollStan, W.; Dshemuchadse, J.; Trapp, N.; Schlüter, A. D. Gram-Scale Synthesis of Two-Dimensional Polymer Crystals and their Structure Analysis by X-ray Diffraction. *Nat. Chem.* **2014**, *6*, 779–784.
11. Novoselov, K.; Jiang, D.; Schedin, F.; Booth, T.; Khotkevich, V.; Morozov, S.; Geim, A. Two-Dimensional Atomic Crystals. *Proc. Natl. Acad. Sci. U.S.A.* **2005**, *102*, 10451–10453.
12. Liu, H.; Hsu, C.-H.; Lin, Z.; Shan, W.; Wang, J.; Jiang, J.; Huang, M.; Lotz, B.; Yu, X.; Zhang, W.-B.; Yue, K.; Cheng, S. Z. D. Two-Dimensional Nanocrystals of Molecular Janus Particles. *J. Am. Chem. Soc.* **2014**, *136*, 10691–10699.
13. Kissel, P.; Erni, R.; Schweizer, W. B.; Rossell, M. D.; King, B. T.; Bauer, T.; Götzinger, S.; Schlüter, A. D.; Sakamoto, J. A Two-Dimensional Polymer Prepared by Organic Synthesis. *Nat. Chem.* **2012**, *4*, 287–291.
14. Zhang, K.-D.; Tian, J.; Hanifi, D.; Zhang, Y.; Sue, A.C.-H.; Zhou, T.-Y.; Zhang, L.; Zhao, X.; Liu, Y.; Li, Z.-T. Toward a

Single-Layer Two-Dimensional Honeycomb Supramolecular Organic Framework in Water. *J. Am. Chem. Soc.* **2013**, *135*, 17913–17918.
15. Blodgett, K. B. Films Built by Depositing Successive Monomolecular Layers on a Solid Surface. *J. Am. Chem. Soc.* **1935**, *57*, 1007–1022.
16. Cai, J.; Ruffieux, P.; Jaafar, R.; Bieri, M.; Braun, T.; Blankenburg, S.; Muoth, M.; Seitsonen, A. P.; Saleh, M.; Feng, X.; Mullen, K.; Fasel, R. Atomically Precise Bottom-Up Fabrication of Graphene Nanoribbons. *Nature* **2010**, *466*, 470–473.
17. Chen, Y.; Li, M.; Payamyar, P.; Zheng, Z.; Sakamoto, J.; Schlüter, A. D. Room Temperature Synthesis of a Covalent Monolayer Sheet at Air/Water Interface Using a Shape-Persistent Photoreactive Amphiphilic Monomer. *ACS Macro Lett.* **2014**, *3*, 153–158.
18. Payamyar, P.; Kaja, K.; Ruiz-Vargas, C.; Stemmer, A.; Murray, D. J.; Johnson, C. J.; King, B. T.; Schiffmann, F.; VandeVondele, J.; Renn, A.; Götzinger, S.; Ceroni, P.; Schütz, A.; Lee, L.-T.; Zheng, Z.; Sakamoto, J.; Schlüter, A. D. Synthesis of a Covalent Monolayer Sheet by Photochemical Anthracene Dimerization at the Air/Water Interface and its Mechanical Characterization by AFM Indentation. *Adv. Mater.* **2014**, *26*, 2052–2058.
19. Kambe, T.; Sakamoto, R.; Hoshiko, K.; Takada, K.; Miyachi, M.; Ryu, J.-H.; Sasaki, S.; Kim, J.; Nakazato, K.; Takata, M.; Nishihara, H. π-Conjugated Nickel Bis(dithiolene) Complex Nanosheet. *J. Am. Chem. Soc.* **2013**, *135*, 2462–2465.
20. Zheng, Z.; Ruiz-Vargas, C. S.; Bauer, T.; Rossi, A.; Payamyar, P.; Schütz, A.; Stemmer, A.; Sakamoto, J.; Schlüter, A. D. Square-Micrometer-Sized, Free-Standing Organometallic Sheets and Their Square-Centimeter-Sized Multilayers on Solid Substrates. *Macromol. Rapid Commun.* **2013**, *34*, 1670–1680.
21. Angelova, P.; Vieker, H.; Weber, N.-E.; Matei, D.; Reimer, O.; Meier, I.; Kurasch, S.; Biskupek, J.; Lorbach, D.; Wunderlich, K.; Chen, L.; Terfort, A.; Klapper, M.; Müllen, K.; Kaiser, U.; Gölzhäuser, A.; Turchanin, A. A Universal Scheme To Convert Aromatic Molecular Monolayers into Functional Carbon Nanomembranes. *ACS Nano* **2013**, *7*, 6489–6497.
22. Liu, X.-H.; Guan, C.-Z.; Ding, S.-Y.; Wang, W.; Yan, H.-J.; Wang, D.; Wan, L.-J. On-Surface Synthesis of Single-Layered Two-Dimensional Covalent Organic Frameworks *via* Solid–Vapor Interface Reactions. *J. Am. Chem. Soc.* **2013**, *135*, 10470–10474.
23. Mueggenburg, K. E.; Lin, X.-M.; Goldsmith, R. H.; Jaeger, H. M. Elastic Membranes of Close-Packed Nanoparticle Arrays. *Nat. Mater.* **2007**, *6*, 656–660.
24. Sanii, B.; Kudirka, R.; Cho, A.; Venkateswaran, N.; Olivier, G. K.; Olson, A. M.; Tran, H.; Harada, R. M.; Tan, L.; Zuckermann, R. N. Shaken, not Stirred: Collapsing a Peptoid Monolayer To Produce Free-Floating, Stable Nanosheets. *J. Am. Chem. Soc.* **2011**, *133*, 20808–20815.
25. Robertson, E. J.; Olivier, G. K.; Qian, M.; Pizano, R.; Proulx, C.; Zuckermann, R. N.; Richmond, G. L. Assembly and Molecular Order of Two-Dimensional Peptoid Nanosheets through the Oil-Water Interface. *Proc. Natl. Acad. Sci. U.S.A.* **2014**, *111*, 13284–13289.
26. Sun, J.; Zuckermann, R. N. Peptoid Polymers: A Highly Designable Bioinspired Material. *ACS Nano* **2013**, *7*, 4715–4732.
27. Reddy, M. M.; Wilson, R.; Wilson, J.; Connell, S.; Gocke, A.; Hynan, L.; German, D.; Kodadek, T. Identification of Candidate IgG Biomarkers for Alzheimer's Disease *via* Combinatorial Library Screening. *Cell* **2011**, *144*, 132–142.
28. Zuckermann, R. N.; Kodadek, T. Peptoids as Potential Therapeutics. *Curr. Opin. Mol. Ther.* **2009**, *11*, 299–307.
29. Zuckermann, R.; Kerr, J.; Kent, S.; Moos, W. Efficient Method for the Preparation of Peptoids [Oligo(N-Substituted Glycines)] by Submonomer Solid-Phase Synthesis. *J. Am. Chem. Soc.* **1992**, *114*, 10646–10647.
30. Tran, H.; Gael, S. L.; Connolly, M. D.; Zuckermann, R. N. Solid-Phase Submonomer Synthesis of Peptoid Polymers and Their Self-Assembly into Highly-Ordered Nanosheets. *J. Visualized Exp.* **2011**, *57*, e3373.
31. Culf, A. S.; Ouellette, R. J. Solid-Phase Synthesis of N-Substituted Glycine Oligomers (α-Peptoids) and Derivatives. *Molecules* **2010**, *15*, 5282–5335.
32. Fowler, S. A.; Blackwell, H. E. Structure-Function Relationships in Peptoids: Recent Advances Toward Deciphering the Structural Requirements for Biological Function. *Org. Biomol. Chem.* **2009**, *7*, 1508–1524.
33. Lau, K. H. A. Peptoids for Biomaterials Science. *Biomater. Sci.* **2014**, *2*, 627–633.
34. Seo, J.; Lee, B.-C.; Zuckermann, R. N. Peptoids: Synthesis, Characterization, and Nanostructures. In *Comprehensive Biomaterials*; Ducheyne, P., Healy, K. E., Hutmacher, D. W., Grainger, D. W., Kirkpatrick, C. J., Eds.; Elsevier: Amsterdam, 2011; Vol. 2, pp 53−76.
35. Yoo, B.; Kirshenbaum, K. Peptoid Architectures: Elaboration, Actuation, and Application. *Curr. Opin. Chem. Biol.* **2008**, *12*, 714–721.
36. Zuckermann, R. N. Peptoid Origins. *Pept. Sci.* **2011**, *96*, 545–555.
37. Zhang, D.; Lahasky, S. H.; Guo, L.; Lee, C.-U.; Lavan, M. Polypeptoid Materials: Current Status and Future Perspectives. *Macromolecules* **2012**, *45*, 5833–5841.
38. Luxenhofer, R.; Fetsch, C.; Grossmann, A. Polypeptoids: A Perfect Match for Molecular Definition and Macromolecular Engineering? *J. Polym. Sci., Part A: Polym. Chem.* **2013**, *51*, 2731–2752.
39. Kudirka, R.; Tran, H.; Sanii, B.; Nam, K. T.; Choi, P. H.; Venkateswaran, N.; Chen, R.; Whitelam, S.; Zuckermann, R. N. Folding of a Single-Chain, Information-Rich Polypeptoid Sequence into a Highly-Ordered Nanosheet. *Peptide Science* **2011**, *96*, 586–595.
40. Nam, K. T.; Shelby, S. A.; Choi, P. H.; Marciel, A. B.; Chen, R.; Tan, L.; Chu, T. K.; Mesch, R. A.; Lee, B. C.; Connolly, M. D.; Kisielowski, C.; Zuckermann, R. N. Free-Floating Ultrathin Two-Dimensional Crystals from Sequence-Specific Peptoid Polymers. *Nat. Mater.* **2010**, *9*, 454–60.
41. Olivier, G. K.; Cho, A.; Sanii, B.; Connolly, M. D.; Tran, H.; Zuckermann, R. N. Antibody-Mimetic Peptoid Nanosheets for Molecular Recognition. *ACS Nano* **2013**, *7*, 9276–9286.
42. Gopal, A.; Lee, K. Morphology and Collapse Transitions in Binary Phospholipid Monolayers. *J. Phys. Chem. B* **2001**, *105*, 10348–10354.
43. Baoukina, S.; Monticelli, L.; Risselada, H. J.; Marrink, S. J.; Tieleman, D. P. The Molecular Mechanism of Lipid Monolayer Collapse. *Proc. Natl. Acad. Sci. U.S.A.* **2008**, *105*, 10803–10808.
44. Fragneto, G.; Charitat, T.; Daillant, J. Floating Lipid Bilayers: Models for Physics and Biology. *Eur. Biophys. J.* **2012**, *41*, 863–874.
45. Haxton, T. K.; Mannige, R. V.; Zuckermann, R. N.; Whitelam, S. Modeling Sequence-Specific Polymers using Anisotropic Coarse-Grained Sites allows Quantitative Comparison with Experiment, **2014** (available online at arxiv.org/abs/1409.8644).
46. Fyfe, M. C.; Stoddart, J. F. Synthetic Supramolecular Chemistry. *Acc. Chem. Res.* **1997**, *30*, 393–401.
47. Glotzer, S. C. Some Assembly Required. *Science* **2004**, *306*, 419–420.
48. Lehn, J.-M. Perspectives in Supramolecular Chemistry, From Molecular Recognition towards Molecular Information Processing and Self-Organization. *Angew. Chem., Int. Ed.* **1990**, *29*, 1304–1319.
49. Yeates, T. O.; Padilla, J. E. Designing Supramolecular Protein Assemblies. *Curr. Opin. Struct. Biol.* **2002**, *12*, 464–470.
50. Serpell, L. C. Alzheimer's Amyloid Fibrils: Structure and Assembly. *Biochim. Biophys. Acta* **2000**, *1502*, 16–30.
51. Rapaport, H.; Kjaer, K.; Jensen, T. R.; Leiserowitz, L.; Tirrell, D. A. Two-Dimensional Order in β-Sheet Peptide Monolayers. *J. Am. Chem, Soc.* **2000**, *122*, 12523–12529.
52. Clark, N. A.; Rothschild, K. J.; Luippold, D. A.; Simon, B. A. Surface-Induced Lamellar Orientation of Multilayer Membrane Arrays. Theoretical Analysis and a New Method with Application to Purple Membrane Fragments. *Biophys. J.* **1980**, *31*, 65–96.
53. Segalman, R. A. Patterning with Block Copolymer Thin Films. *Mater. Sci. Eng., R* **2005**, *48*, 191–226.

54. Vollhardt, D.; Melzer, V. Phase Transition in Adsorption Layers at the Air-Water Interface: Bridging to Langmuir Monolayers. *J. Phys. Chem. B* **1997**, *101*, 3370–3375.
55. Grubb, D. Radiation Damage and Electron Microscopy of Organic Polymers. *J. Mater. Sci.* **1974**, *9*, 1715–1736.
56. Blair, H. S.; Pague, H. I.; Riordan, J. E. Photoresponsive Effects in Azo Polymers. *Polymer* **1980**, *21*, 1195–1198.
57. Mmereki, B. T.; Donaldson, D. Direct Observation of the Kinetics of an Atmospherically Important Reaction at the Air-Aqueous Interface. *J. Phys. Chem. A* **2003**, *107*, 11038–11042.
58. Metropolis, N.; Rosenbluth, A. W.; Rosenbluth, M. N.; Teller, A. H.; Teller, E. Equation of State Calculations by Fast Computing Machines. *J. Chem. Phys.* **1953**, *21*, 1087–1092.
59. Chantler, C. T. Theoretical Form Factor, Attenuation, and Scattering Tabulation for Z = 1−92 from E = 1−10 eV to E = 0.4−1.0 MeV. *J. Phys. Chem. Ref. Data* **1995**, *24*, 71–643.